

# Gigantic-oxidative atomically layered epitaxy for designed complex oxides

Guangdi Zhou<sup>1#</sup>, Haoliang Huang<sup>1,2#</sup>, Fengzhe Wang<sup>1</sup>, Heng Wang<sup>1</sup>, Qishuo Yang<sup>1</sup>, Zihao Nie<sup>1</sup>, Wei Lv<sup>1</sup>, Cui Ding<sup>2</sup>, Yueying Li<sup>1</sup>, Danfeng Li<sup>2,3</sup>, Yujie Sun<sup>1,2</sup>, Junhao Lin<sup>1,2</sup>, Guang-Ming Zhang<sup>4,5</sup>, Qi-Kun Xue<sup>1,2\*</sup>, Zhuoyu Chen<sup>1,2\*</sup>

<sup>1</sup>Department of Physics, Southern University of Science and Technology, Shenzhen, China

<sup>2</sup>Quantum Science Center of Guangdong-Hong Kong-Macao Greater Bay Area, Shenzhen, China

<sup>3</sup>Department of Physics, City University of Hong Kong, Kowloon, Hong Kong

<sup>4</sup>State Key Laboratory of Low-Dimensional Quantum Physics, Department of Physics, Tsinghua University, Beijing, China

<sup>5</sup>Frontier Science Center for Quantum Information, Beijing, China

#These authors contributed equally.

\*E-mail: [xueqk@sustech.edu.cn](mailto:xueqk@sustech.edu.cn), [chenzhuoyu@sustech.edu.cn](mailto:chenzhuoyu@sustech.edu.cn)

**In designing material functionality within the intricate realm of transition metal oxides, lattice structure and *d*-orbital occupancy are two principal determinants of the correlated physical properties, such as superconductivity<sup>1-3</sup>. However, the modulation of these two factors is inherently limited by the need to balance thermodynamic stability, kinetic mobility, and synthesis precision, particularly for oxidation-demanding phases<sup>4,5</sup>. We introduce a methodology, namely the gigantic-oxidative atomically layered epitaxy (GOAL-Epitaxy), enhancing oxidation power 3-4 orders of magnitude beyond oxide molecular beam epitaxy (OMBE) and pulsed laser deposition (PLD), while ensuring atomic-layer-by-layer growth of designed complex structures<sup>6-8</sup>. Consequently, thermodynamic stability is markedly augmented at elevated temperatures, improving growth kinetics. We demonstrate the accurate synthesis of complex nickelates and cuprates, especially an artificially designed structure as a parent of high-temperature superconductivity, in which alternating single and double NiO<sub>2</sub> layers possess distinct nominal *d*-orbital occupancy<sup>9</sup>. The GOAL-Epitaxy enables material discovery within the vastly broadened growth parameter space.**

Electron correlations in transition metal oxides weave complex entanglements among charge, spin, orbital, and lattice degrees of freedom, giving rise to a rich spectrum of phenomena, including metal-insulator transitions, diverse charge, spin, and orbital orderings, multiferroics, and superconductivity<sup>1,2</sup>. These intertwined orders are rooted in the delicate balance of similar, yet competing and correlated energy scales<sup>3</sup>. For instance, the transition from metal to magnetic insulator depends on the comparison between the  $d$ -orbital bandwidth and the  $d$ - $d$  Coulomb interaction. Further complexity arises if the oxygen ligand-to-metal charge transfer energy falls below the Coulomb interaction, shifting the determination to this finer energy scale compared to bandwidth<sup>10</sup>. This nuanced energy landscape underscores the diverse manifestations of physical states in transition metal oxides, setting the stage for the design of correlated electron systems.

In the design of complex oxides with desired functionalities or physical properties, the two important dimensions of consideration are lattice structure and  $d$ -orbital occupancy of transition metal ions. Lattice structure, encompassing single crystals, heterostructures, and superlattices, not only determines the dimensionality of the active functional layer (e.g. 3D versus 2D) but also governs interfacial coupling between layers within the designed structures<sup>11-13</sup>. Simultaneously, the number of correlated electrons residing in the  $d$  orbitals at each lattice site directly links to the electronic structure and Fermi level of the system<sup>14-16</sup>. However, the interplay between lattice structure and  $d$ -orbital occupancy is complex and often interdependent<sup>17,18</sup>. Perturbations of the lattice structures, such as oxygen octahedra rotation<sup>13,19,20</sup> or Jahn-Teller distortion<sup>21</sup>, are closely related to the electron count in  $d$  orbitals due to crystal field anisotropy, illustrating the intricate relationship between these fundamental parameters.

The successful synthesis of designed systems hinges on two critical abilities: (1) the independent control over the intertwined factors of lattice structure and transition metal  $d$ -orbital occupancy, and (2) the stabilization and manipulation of metastable phases of complex oxides. Achieving these objectives necessitates careful attention to thermodynamic stability, growth kinetic mobility, stoichiometry precision, and the ability to accurately control oxygen content *in situ*. OMBE and PLD stand out as premier techniques for crafting complex oxide epitaxial single-crystalline thin films and heterostructures<sup>6,7</sup>. While these thin film techniques facilitate the creation of artificial structures and enable the exploration of complex physical phenomena through the manipulation of multiple degrees of

freedom, their effectiveness is somewhat diminished for phases that demand significant oxidation, compared to methods like high-pressure synthesis<sup>22,23</sup>. OMBE, especially when employing alternately shuttered element sources, offers meticulous control over cation stoichiometry and supports atomic-layer-by-layer growth<sup>24-26</sup>, whereas PLD is prized for its simplicity, versatility of materials, and capability for higher pressure environments to enhance thermodynamic stability<sup>4,5</sup>. Nonetheless, each technique faces its challenges: OMBE is limited by the vapor pressure of elements and requires a low-pressure environment for the transport of evaporated materials to the substrate, thus constraining its oxidation potential; PLD can lead to stoichiometric imbalances and is less effective for materials with complex and large unit cells, such as Ruddlesden-Popper (RP) phases. Addressing these comprehensive requirements, we present the gigantic-oxidative atomically layered epitaxy (GOAL-Epitaxy) method, detailed subsequently.

Figure 1 illustrates the operational principles of GOAL-Epitaxy with a prominent example synthesis of an artificially designed nickelate structure as a parent for high-temperature superconductivity<sup>9</sup>. Consist of La, Ni, and O, this structure features the alternating stacking of single- and double-layer NiO<sub>2</sub> planes (thus denoted “1212”), with nominal  $3d^8$  and  $3d^{7.5}$  occupancy, respectively (Figure 1a). The 1212 structure can be regarded as a combination of La<sub>2</sub>NiO<sub>4</sub> and La<sub>3</sub>Ni<sub>2</sub>O<sub>7</sub> RP phases, the former of which is an antiferromagnetic insulator and the latter of which was recently found to host superconductivity at liquid nitrogen temperatures<sup>23</sup>. The 1212 structure does not belong to the RP series and is particularly difficult to stabilize thermodynamically, since Ni in La<sub>2</sub>NiO<sub>4</sub> and La<sub>3</sub>Ni<sub>2</sub>O<sub>7</sub> has different valence, and thus in principle requires different oxidation power for growth. Nonetheless, thanks to the flexibility of GOAL-Epitaxy, the 1212 structure can be well realized in thin film form as shown by the scanning transmission electron microscopy (STEM) image with atom positions identified in Figure 1b.

In general, upon receiving a task of synthesis, the designed structure is broken down into its constituent oxide atomic layers (LaO and NiO<sub>2</sub>, in this case, schematized in Figure 1c). Each atomic layer is associated with a specific oxide target (i.e. LaO<sub>x</sub> and NiO<sub>x</sub>). After setting the optimal growth temperature and oxidation conditions, atomic layers are successively deposited onto a chosen substrate through pulsed laser ablation of these oxide targets<sup>6,8</sup>. The number of pulses required for each complete layer, varying from a few tens to several

hundreds, is determined by the properties of the target material and the selected laser energy. Layers are deposited in a programmed sequence that reflects the design, with the entire growth process monitored in real-time by reflective high-energy electron diffraction (RHEED), allowing for the immediate capture of elemental and layer completion characterization data<sup>27</sup>, facilitating the atomic-layer-by-layer growth mode<sup>7,8,28-31</sup>. In the example case of 1212 structure, one RHEED oscillation cycle corresponds to one LaO-NiO<sub>2</sub>-LaO-NiO<sub>2</sub>-LaO (a double-NiO<sub>2</sub> layer) block plus one LaO-NiO<sub>2</sub>-LaO (a single-NiO<sub>2</sub> layer) block, realized by sequentially depositing using LaO<sub>x</sub>, NiO<sub>x</sub>, LaO<sub>x</sub>, NiO<sub>x</sub>, LaO<sub>x</sub>, and LaO<sub>x</sub>, NiO<sub>x</sub>, LaO<sub>x</sub> targets.

Expanding upon atomic-layer-by-layer growth, the GOAL-Epitaxy technique employs purified ozone with a specially designed ozone nozzle (1/2 inch inner diameter) aimed directly at the sample, positioned closely (~4 cm) to establish a highly concentrated oxidation zone close to the substrate (see Figure S1 for simulation analysis). This configuration amplifies oxidation power by around half order of magnitude, a crucial enhancement given the rapid decomposition of ozone molecules upon contact with the heated sample stage. The ozone gas is purified in a liquefaction unit positioned close to the chamber's ozone inlet to minimize decomposition during transport. The RHEED is equipped with a two-stage differentially pump system, enabling atomic-layer-by-layer growth mode to sustain ozone chamber pressures up to 0.1 mbar. In contrast to OMBE, GOAL-Epitaxy synergizes the high-energy plasma plume generated by laser pulses—capable of withstanding high chamber ozone pressures for effective material transport to the substrate. Under strong oxidative conditions, GOAL-Epitaxy's theoretical stoichiometry is as precise as 0.1%, and experimentally demonstrated to be no worse than 0.3% (see Figure S2). Additionally, the chamber pressure can be tuned in accordance with the laser fluence to ensure that ablated particles reach the substrate surface with a suitable kinetic energy, causing neither excessive damage to the grown structure nor insufficient surface diffusion. In the example case of 1212 structure, the oxidative environment was meticulously set to  $4 \times 10^{-4}$  mbar ozone plus  $9.6 \times 10^{-3}$  mbar oxygen with laser fluence 1.4 J/cm<sup>2</sup> for both LaO<sub>x</sub> and NiO<sub>x</sub> targets (generally laser fluence can be different for different targets). For nominally distinct valences of nickel in different phases, the growth in principle necessitates different oxidative strengths. The mixed oxygen-ozone condition is chosen to accommodate both the growth of single-layer and double-

layer structures. Full oxidative power was used for  $\text{LaNiO}_3$  to be discussed in Figure 2.

STEM high-angle annular dark field (HAADF) image with a larger field of view (Figure 1d) shows coherent 1212 lattice structure with a sharp substrate/film interface. Atomically resolved energy-dispersive X-ray spectroscopy (EDS) images exhibit elemental selective signals (Figure 1e). Within the field of view shown and all other EDS images measured (not shown here), we did not observe interdiffusion of Al and Ni atoms at the interface. On top of the atomically flat substrate, single and double layer of Ni is alternatively stacked, signifying the high-quality realization of the artificially designed complex oxide lattice. X-ray diffraction (XRD, Figure 1f) displays nearly all predicted peaks within measurable range, except for those overlapping with substrate peaks and (0024) due to lower symmetry. Low-temperature resistivity measurement of our grown film exhibits pure insulating behavior, in contrast to that of bulk crystal<sup>9</sup> featuring a down bending below 140 K.

Figures 2a to 2e illustrate RP phases with varying numbers of transition metal oxide layers—using Ni as an example due to its high oxidation requirements. These variations correspond to different  $3d$  orbital occupancy (Figure 2a). Since carrier transport occurs within  $\text{NiO}_2$  layers, the number of stacking layers controls the effective dimensionality of the electronic system: Between adjacent blocks,  $\text{NiO}_2$  layers are separated by two insulating LaO layers and the alignment of the oxygen octahedra in the lattice is shifted by approximately one bond length, reducing the probability of carrier hopping. The RHEED oscillations (Figure 2b) reveal that different sequences of ablating La and Ni (i.e.,  $\text{LaO}_x$  and  $\text{NiO}_x$  targets) yield various structural designs, with steady oscillation intensity indicating stoichiometric growth (example RHEED patterns shown in Figure S3). The XRD spectrum for each structure (Figure 2c) shows consecutive Bragg peaks along the out-of-plane axis, confirming periodic lattice structures. An STEM image of the two-layer structure  $\text{La}_3\text{Ni}_2\text{O}_7$  (Figure 2d) confirms the coherent growth on the  $\text{LaAlO}_3$  substrate and alternately positioned LaO- $\text{NiO}_2$ -LaO- $\text{NiO}_2$ -LaO blocks. Systematic resistivity-temperature curves for different layer stacking configurations (Figure 2e) reveal that while infinite-layer  $\text{LaNiO}_3$  displays metallic behavior, structures with 5 to 2 layers exhibit a metal-insulator transition at low temperatures, likely due to reduced dimensionality. The resistivity tends to increase as the number of layers decreases, largely a result of changes of electron occupancy in the  $3d$  orbitals, with the single-layer case ( $\text{La}_2\text{NiO}_4$ ) being highly

insulating, aligning with prior findings<sup>30,31</sup>. The enhancements in growth thermodynamics and kinetics provided by GOAL-Epitaxy enable the extension of the growth temperature range for LaNiO<sub>3</sub>. Specifically, the lower temperature limit is extended to 350 °C under a chamber pressure of  $2 \times 10^{-5}$  mbar of O<sub>3</sub>, while the upper temperature limit reaches 900 °C at a chamber pressure of 0.1 mbar of O<sub>3</sub> (see Figure S4). The quality of LaNiO<sub>3</sub> growth enables a wide tunable range of in-plane coherent strain reaching up to 4.5% (see Figure S5).

Upon synthesizing the designed general structure, for independent control of transition metal *d*-orbital occupancy over wide ranges while keeping structural coherence, we implement *in situ* reduction via atomic hydrogen in a dedicated reduction chamber, as illustrated in Figure S6a. The thermally activated atomic hydrogen source is positioned vertically ~20 cm below the sample, to ensure a consistent flux ( $\sim 3 \times 10^{15}$  atoms/cm<sup>2</sup>s) across the sample surface, important for achieving a spatially uniform reduction rate. XRD data presented in Figure S6b demonstrate the capability to precisely adjust oxygen content from (La,Sr)NiO<sub>3</sub> with approximately  $3d^{6.8}$  configuration, to (La,Sr)NiO<sub>2</sub>, corresponding to around  $3d^{8.8}$ , by varying atomic hydrogen flux and annealing temperature. Besides atomic hydrogen, reduction through deposition of a thin reductant metal layer, such as evaporated Al from an effusion cell<sup>32</sup>, is also possible in our reduction chamber.

The next example showcases the synthesis of infinite-layer cuprate structures, with maximized oxidation power of GOAL-Epitaxy (Figure 3a). The infinite-layer structure represents the most fundamental parent of cuprate superconductors, characterized by the uninterrupted stacking of CuO<sub>2</sub> planes, interspersed with alkaline earth ions<sup>33,34</sup>. Mastering the synthesis and manipulation of this structure is crucial for designing and creating new cuprate superconductors, although producing high-quality crystals faces significant challenges due to their thermodynamic metastable nature<sup>5,8</sup>. Achieving their synthesis necessitates exceptionally strong oxidation conditions: a more powerful oxidation environment promotes thermodynamic stability at elevated growth temperatures, thus enhancing kinetic growth mobility and resulting in higher crystalline quality. In previous experiments using OMBE and PLD, the growth temperature typically ranged between 550-600°C due to limited oxidation capabilities<sup>8,35-37</sup>. By utilizing near-maximum oxidation strength achievable with GOAL-Epitaxy, stable growth of infinite-layer cuprates has been achieved at temperatures between 600-700 °C, markedly exceeding those of earlier methods. In Figure 3b,

an STEM image demonstrates the coherent  $\text{CaCuO}_2$  thin film on the  $\text{NdGaO}_3$  substrate, showcasing the potential for precise control and manipulation of these structures. Figure 3c shows three example growth process of  $\text{CaCuO}_2$  (with  $\text{SrCuO}_2$  buffer),  $\text{Sr}_{0.5}\text{Ca}_{0.5}\text{CuO}_2$  (with  $\text{SrCuO}_2$  buffer), and  $\text{SrCuO}_2$ . Intriguingly, to achieve a 1:1 stoichiometry between Sr and Ca in  $\text{Sr}_{0.5}\text{Ca}_{0.5}\text{CuO}_2$ , we alternate the deposition of one atomic layer of Sr with one atomic layer of Ca, thus one cycle of RHEED oscillation corresponds to the formation of two unit cells. XRD data (Figure 3d) reveal systematic variations in the out-of-plane lattice constant with different alkaline-earth element compositions. The slender reciprocal spots confirm the crystallinity of these cuprate thin films prepared by GAOL-Epitaxy (Figure 3e).

Figure 4 summarizes the parameter space covered by various oxide thin film techniques and the parameters required for different material systems. GOAL-Epitaxy exhibits oxidation power significantly surpassing conventional PLD by three orders of magnitude and OMBE by four, enhancing thermodynamic stability considerably. Their upper pressure limits are determined by evaporation mean free paths for OMBE, deposition rate of ablated materials for PLD, and availability of RHEED for GOAL-Epitaxy. Regarding lower temperature limits, while PLD provides higher kinetic energy to deposited materials by laser ablation compared to OMBE at lower evaporation temperatures, GOAL-Epitaxy's laser ablated high kinetics are primarily required and utilized within single atomic layer ranges during growth, offering further flexibility for lower temperatures compared to the unit cell ranges for PLD. At higher temperatures, both GOAL-Epitaxy and OMBE are mainly limited by substrate heater capacity (laser heater versus typical resistive radiation), while PLD also considers heat dissipation at higher pressure. The distinct growth parameter regimes for nickelates (represented by  $\text{ReNiO}_3$ , where Re = rare earth), infinite-layer cuprates, and finite-layer cuprates (e.g.  $\text{La}_2\text{CuO}_4$  and  $\text{YBa}_2\text{Cu}_3\text{O}_{7-\delta}$ ) involves both thermodynamic and kinetic considerations. The near-vertical boundary at lower temperatures represents a kinetic limitation: for instance, more complex and larger unit cells in finite-layer cuprates (e.g.  $\text{YBa}_2\text{Cu}_3\text{O}_{7-\delta}$ ) requires higher kinetic thresholds for lattice formation, comparing to infinite-layer cuprates. The boundary at higher temperatures is determined by thermodynamic constraints, with greater oxidation power providing increased thermodynamic stability at elevated growth temperatures<sup>38</sup>.

Finite-layer cuprates can be synthesized more readily using conventional PLD or OMBE, thanks to their broad overlapping parameter spaces. However, the overlapping parameter spaces for nickelates and infinite-layer cuprates are significantly narrower, considerably limiting opportunities for optimization and the exploration of new phases and structures. In contrast, GOAL-Epitaxy's expanded parameter space offers significant advantages for the design and discovery of new materials. The superior oxidation capabilities support higher growth temperatures, which in turn enhance crystallinity by higher growth kinetics within single atomic layers. Additionally, GOAL-Epitaxy achieves atomic-layer precision—on par with OMBE and exceeding the unit cell precision in conventional PLD—thereby optimizing synthesis precision while preserving material versatility.

In conclusion, GOAL-Epitaxy marks a significant leap in complex oxide thin film techniques, broadening the research landscape to previously uncharted parameter spaces. It not only amalgamates the strengths of both OMBE and PLD while overcoming their limitations, but also surpasses them substantially. The simultaneous achievements of ultrastrong oxidative power and sub-atomic-layer control precision enable the rational construction of artificially designed complex oxide structures with higher kinetics under significantly enhanced thermodynamic stability. The integration of potent oxidation and reduction capabilities into a unified ultrahigh vacuum interconnected system also offers crucial flexibility of independent and soft oxygen content control, enabling wide-range tuning of *d*-orbital occupancy besides cation substitutions, without compromising structural integrity. GOAL-Epitaxy vastly expands the design scope of strongly correlated electron systems with tailored functionalities, such as higher- $T_C$  superconductors, highlighting a transformative impact on the synthesis of complex oxide materials.

## Methods

**Nickelate Ruddlesden-Popper (RP) phases growth.** Growth temperatures are typically set between 550 °C and 800 °C, with ozone chamber pressures ranging from  $1 \times 10^{-5}$  mbar to 0.1 mbar.  $\text{LaO}_x$  and  $\text{NiO}_x$  targets are alternatively ablated using a KrF excimer laser ( $\lambda = 248$  nm, pulse duration 25 ns) for the sequential growth of different atomic layers. Stoichiometry control for various RP phases,



encompassing the required pulse numbers for each atomic layer's completion and the laser energy, is initially calibrated using LaNiO<sub>3</sub> film synthesis and subsequently fine-tuned. During deposition, typically the laser fluence on the LaO<sub>x</sub> and NiO<sub>x</sub> targets was ~1.4 J/cm<sup>2</sup> at 2 Hz and ~1.4 – 1.8 J/cm<sup>2</sup> at 2 Hz, respectively. The typical number of laser pulses was about 90 for each LaO layer and 100 for each NiO<sub>2</sub> layer. In case of Sr doping, (La,Sr)O<sub>x</sub> target was used instead of LaO<sub>x</sub>, in which Sr ratio is around 0.2. All growth of thin films is monitored in real-time using 30 keV RHEED. Substrates mounted on a flag-type sample holder are heated by laser with highest temperature exceeding 1100 °C.

**Atomic hydrogen reduction.** The as-grown (La,Sr)NiO<sub>3</sub> films without any capping were *in situ* transferred under ultrahigh vacuum from the oxidation growth chamber into a dedicated reduction chamber. The atomic hydrogen were generated by a commercial hydrogen sources from Dr. Eberl MBE-Komponenten GmbH. For different levels of oxygen content, the reaction temperature ranges from 250 °C to 300 °C and the flux ranges from 0.5 to 3 × 10<sup>15</sup> atoms/cm<sup>2</sup>s.

**Infinite-layer cuprate growth.** The infinite-layer cuprate films were grown on an (001)-oriented SrTiO<sub>3</sub>, or 0.05% Nb doped SrTiO<sub>3</sub>, or NdGaO<sub>3</sub> single-crystal substrate with a KrF excimer laser ( $\lambda = 248$  nm, pulse duration 25 ns). During deposition, the laser fluence on the ceramic SrO<sub>x</sub> and CaO<sub>x</sub> targets was 0.6 J/cm<sup>2</sup> at 2 Hz, and on the ceramic CuO<sub>x</sub> targets was 1.9 J/cm<sup>2</sup> at 2 Hz. The oxygen partial pressure was set to 1-2×10<sup>-2</sup> mbar, and the substrate temperature was maintained from 600 °C to 750 °C. The typical number of laser pulses was about 200 for each CaO<sub>x</sub> layer, 60 for each SrO<sub>x</sub> layer, and 80 for each CuO<sub>x</sub> layer in the growth of stoichiometric CaCuO<sub>2</sub>, SrCuO<sub>2</sub>, and Sr<sub>0.5</sub>Ca<sub>0.5</sub>CuO<sub>2</sub>. After deposition, the SrCuO<sub>2</sub> and Sr<sub>0.5</sub>Ca<sub>0.5</sub>CuO<sub>2</sub> films were annealed at about 1×10<sup>-7</sup> mbar under 520 °C for 10 min, and the CaCuO<sub>2</sub> films were cooled down to room temperature at a rate of 10 °C/min at growth oxygen partial pressure. All growth of thin films is monitored in real-time using 30 keV RHEED. Substrates mounted on a flag-type sample holder are heated by laser with highest temperature exceeding 1100 °C.

**Target preparation.** CaO<sub>x</sub>, SrO<sub>x</sub>, and LaO<sub>x</sub> targets are reactive in ambient atmospheres, forming hydroxides upon contact with water, while LaO<sub>x</sub> additionally absorbs CO<sub>2</sub> from the air. To mitigate these reactions, these targets were sintered in a furnace within a glovebox under a dry Ar atmosphere. They

were then mounted onto the target holders and rapidly transferred to the vacuum chamber through a load-lock system to minimize their exposure to air.

**Substrate preparation.** To achieve sharp step and terrace surfaces on TiO<sub>2</sub>-terminated SrTiO<sub>3</sub> (001) substrates (Shinkosha, Japan), annealing processes were executed at 1100 °C for a protracted period of 6 hours within an air atmosphere. For the LaAlO<sub>3</sub> (001) substrates (MTI, China), an initial pre-treatment entailed immersion in boiling deionized water for 15 minutes. Subsequent annealing was performed under identical temperature, time and atmospheric conditions as SrTiO<sub>3</sub>. The substrates were subjected to a repeated deionized water treatment-annealing protocol when needed, effectively yielding AlO<sub>2</sub>-terminated LaAlO<sub>3</sub> substrates.

**X-ray diffraction (XRD).** Crystallographic characterization of thin-film specimens was performed by SmartLab, an automated multipurpose X-ray diffractometer, from Rigaku Corporation, encompassing theta-2theta scans and RSM.

**Scanning transmission electron microscopy (STEM).** STEM HAADF imaging of La<sub>3</sub>Ni<sub>2</sub>O<sub>7</sub> and CaCuO<sub>2</sub> was photographed using a FEI Titan Themis G2 at 300 kV, with a double spherical-aberration corrector (DCOR) and a high-brightness field-emission gun (X-FEG) with a monochromator is installed onto this microscope. The inner and outer collection angles for the STEM images ( $\beta_1$  and  $\beta_2$ ) were 48 and 200 mrad, respectively, with a semi-convergence angle of 25 mrad. The beam current was about 80 pA for high-angle annular dark-field imaging and the EDS chemical analyses. All imaging was done at room temperature. The cross-section STEM specimens of La<sub>3</sub>Ni<sub>2</sub>O<sub>7</sub> and CaCuO<sub>2</sub> were prepared using a FEI Helios 600i dual-beam FIB/SEM machine. Before extraction and thinning, we used electron beam-deposited platinum and ion beam-deposited carbon to protect the sample surface from ion beam damage. The cross-section STEM specimen of the 1212 structure was prepared using a Thermo Scientific Helios G4 HX machine, and was protected by electron beam-deposited platinum and ion beam-deposited carbon before extraction and thinning. The STEM annular bright field (ABF) and HAADF imaging of 1212 structure was photographed using a Thermo Scientific Themis Z at 200 kV with spherical-aberration corrector. And EDS data of 1212 structure were obtained using the Super X FEI System in STEM mode.

**Low-temperature transport measurements.** Electric transport measurements were performed in a closed-cycle helium-free system (base temperature below 1.5K). The four terminal electrical measurements were carried out through either the standard lock-in technique with an AC current of 1  $\mu$ A (13.333 Hz) or a Keithley 6221 current source and 2182A voltmeter in a delta mode configuration.

## Data availability

All data that support the findings of this study are available within the paper and its Supplementary information. Source data are provided upon request to the corresponding authors.

## References

1. Hwang, H., Iwasa, Y., Kawasaki, M. *et al.* Emergent phenomena at oxide interfaces. *Nature Mater.* **11**, 103–113 (2012).
2. Keimer, B., Kivelson, S., Norman, M. *et al.* From quantum matter to high-temperature superconductivity in copper oxides. *Nature* **518**, 179–186 (2015).
3. Fradkin, E., Kivelson, S.A., Tranquada J.M., Colloquium: Theory of intertwined orders in high temperature superconductors. *Rev. Mod. Phys.* **87**, 457 (2015).
4. Li, D., Lee, K., Wang, B.Y. *et al.* Superconductivity in an infinite-layer nickelate. *Nature* **572**, 624–627 (2019).
5. Castro, D. D., *et al.* High- $T_C$  Superconductivity at the Interface between the  $\text{CaCuO}_2$  and  $\text{SrTiO}_3$  Insulating Oxides. *Phys. Rev. Lett.* **115**, 147001 (2015).
6. Kanai, M., Kawai, T., Kawai, S., & Tabata, H. Low-temperature formation of multilayered Bi (Pb)-Sr-Ca-Cu-O thin films by successive deposition using laser ablation. *Appl. Phys. Lett.* **54**, 1802-1804 (1989).
7. Eckstein, J. N.; Bozovic, I.; von Dessenbeck, K. E.; Schlom, D. G.; Harris, J. S.; Baumann, S. M. Atomically layered heteroepitaxial growth of single-crystal films of superconducting  $\text{Bi}_2\text{Sr}_2\text{Ca}_2\text{Cu}_3\text{O}_x$ . *Appl. Phys. Lett.* **57**, 931 (1990).
8. Matunari, S., Kanai, M., & Kawai, T. Preparation of superconductive  $(\text{BaMO}_x)(\text{BaCuO}_{2+y})(\text{CaCuO}_2)_n$  artificial lattices (M= Au, Cu;  $n= 2, 4$ ) by laser molecular beam epitaxy. *Physica C: Superconductivity* **253**, 217-224 (1995).
9. Li, F., Guo, N., Zheng, Q. *et al.* Design and synthesis of three-dimensional hybrid Ruddlesden-Popper nickelate single crystals. *Phys. Rev. Mater.* **8**, 053401 (2024).
10. Zaanen, J., Sawatzky, G. A., Allen, J. W. Band gaps and electronic structure of transition-metal compounds. *Phys. Rev. Lett.* **55**, 418 (1985).
11. Domínguez, C., Georgescu, A.B., Mundet, B. *et al.* Length scales of interfacial coupling between metal and insulator phases in oxides. *Nat. Mater.* **19**, 1182–1187 (2020).

12. Hoglund, E.R., Bao, D.L., O'Hara, A. *et al.* Emergent interface vibrational structure of oxide superlattices. *Nature* **601**, 556–561 (2022).
13. Liao, Z., Huijben, M., Zhong, Z. *et al.* Controlled lateral anisotropy in correlated manganite heterostructures by interface-engineered oxygen octahedral coupling. *Nature Mater.* **15**, 425–431 (2016).
14. Paschen, S., Si, Q. Quantum phases driven by strong correlations. *Nat. Rev. Phys.* **3**, 9–26 (2021).
15. Chen, Z., Wang, Y. *et al.* Anomalously strong near-neighbor attraction in doped 1D cuprate chains. *Science* **373**, 1235–1239 (2021).
16. Cui, Z.H., Zhai, H.C., Zhang, X. *et al.* Systematic electronic structure in the cuprate parent state from quantum many-body simulations. *Science* **377**, 1192–1198 (2022).
17. Liao, Z., Skoropata, E., Freeland, J.W. *et al.* Large orbital polarization in nickelate-cuprate heterostructures by dimensional control of oxygen coordination. *Nat. Commun.* **10**, 589 (2019).
18. Trier, F., Noël, P., Kim, J.V. *et al.* Oxide spin-orbitronics: spin–charge interconversion and topological spin textures. *Nat. Rev. Mater.* **7**, 258–274 (2022).
19. Zhai, X., Cheng, L., Liu, Y. *et al.* Correlating interfacial octahedral rotations with magnetism in  $(\text{LaMnO}_{3+\delta})_N/(\text{SrTiO}_3)_N$  superlattices. *Nat. Commun.* **5**, 4283 (2014).
20. Hong, Y., Byeon, P., Bak, J. *et al.* Local-electrostatics-induced oxygen octahedral distortion in perovskite oxides and insight into the structure of Ruddlesden–Popper phases. *Nat. Commun.* **12**, 5527 (2021).
21. Kim, W.J., Smeaton, M.A., Jia, C. *et al.* Geometric frustration of Jahn–Teller order in the infinite-layer lattice. *Nature* **615**, 237–243 (2023).
22. Zhang, L., Wang, Y., Lv, J. *et al.* Materials discovery at high pressures. *Nat. Rev. Mater.* **2**, 17005 (2017).
23. Sun, H., Huo, M., Hu, X. *et al.* Signatures of superconductivity near 80 K in a nickelate under high pressure. *Nature* **621**, 493–498 (2023).
24. Logvenov, G., Gozar, A., & Bozovic, I. High-temperature superconductivity in a single copper-oxygen plane. *Science* **326**, 699–702 (2009).
25. Nie, Y., Zhu, Y., Lee, C. H. *et al.* Atomically precise interfaces from non-stoichiometric deposition. *Nat Commun.* **5**, 4530 (2014).
26. Božović, I., He, X., Wu, J., & Bollinger, A. T. Dependence of the critical temperature in overdoped copper oxides on superfluid density. *Nature* **536**, 309–311 (2016).
27. Sun, H.Y., Mao, Z.W., Zhang, T.W. *et al.* Chemically specific termination control of oxide interfaces via layer-by-layer mean inner potential engineering. *Nat. Commun.* **9**, 2965 (2018).
28. Lei, Q., Golalikhani, M., Davidson, B.A. *et al.* Constructing oxide interfaces and heterostructures by atomic layer-by-layer laser molecular beam epitaxy. *npj Quant. Mater.* **2**, 10 (2017).
29. Golalikhani, M., Lei, Q., Chandrasena, R.U. *et al.* Nature of the metal-insulator transition in few-unit-cell-thick  $\text{LaNiO}_3$  films. *Nat Commun.* **9**, 2206 (2018).
30. Pietro, P. D., Golalikhani, M., Wijesekara, K. *et al.* Spectroscopic Evidence of a Dimensionality-Induced Metal-to Insulator Transition in the Ruddlesden–Popper  $\text{La}_{n+1}\text{Ni}_n\text{O}_{3n+1}$  Series. *ACS Appl. Mater. Interfaces* **13**, 6813–6819 (2021).
31. Li, Z., Guo, W., Zhang, T. T. *et al.* Epitaxial growth and electronic structure of Ruddlesden–Popper nickelates  $(\text{La}_{n+1}\text{Ni}_n\text{O}_{3n+1}, n = 1–5)$ . *APL Mater.* **8**, 091112 (2020).

32. Wei, W., Vu, D., Zhang, Z. *et al.* Superconducting  $\text{Nd}_{1-x}\text{Eu}_x\text{NiO}_2$  thin films using in situ synthesis. *Sci. Adv.* **9**, eadh3327 (2023).
33. Smith, M. G., Manthiram, A., Zhou, J. *et al.* Electron-doped superconductivity at 40 K in the infinite-layer compound  $\text{Sr}_{1-y}\text{Nd}_y\text{CuO}_2$ , *Nature* **351**, 549 (1991).
34. Azuma, M., Hiroi, Z., Takano, M. *et al.* Superconductivity at 110 K in the infinite-layer compound  $(\text{Sr}_{1-x}\text{Ca}_x)_{1-y}\text{CuO}_2$ , *Nature* **356**, 775 (1992).
35. Norton, D. P. *et al.* Superconductivity in  $\text{SrCuO}_2$ - $\text{BaCuO}_2$  superlattices: formation of artificially layered superconducting materials. *Science* **265**, 2074-2077 (1994).
36. Harter, J. W., Maritato, L., Shai, D. E. *et al.* Nodeless Superconducting Phase Arising from a Strong  $(\pi, \pi)$  Antiferromagnetic Phase in the Infinite-Layer Electron-Doped  $\text{Sr}_{1-x}\text{La}_x\text{CuO}_2$  Compound, *Phys. Rev. Lett.* **109**, 267001 (2012).
37. Fan, J. Q. *et al.* Direct observation of nodeless superconductivity and phonon modes in electron-doped copper oxide  $\text{Sr}_{1-x}\text{Nd}_x\text{CuO}_2$ . *National Science Review* **9**, nwab225 (2022).
38. Krockenberger, Y., Ikeda, A., Kumakura, K. *et al.* Infinite-layer phase formation in the  $\text{Ca}_{1-x}\text{Sr}_x\text{CuO}_2$  system by reactive molecular beam epitaxy. *J. Appl. Phys.* **124**, 073905 (2018).

## Author contributions

G.Z., W.L., and Z.N. performed synthesis of nickelate thin films. H.H., F.W., and Y.L. performed synthesis of cuprate thin films. H.W. and C.D. performed reduction of nickelate films. H.W. and Z.N. performed low-temperature transport measurements. Q.Y. and J.L. provided STEM imaging. Y.S., D.L., and all other authors participated discussions. G.M.Z. designed material structures. Z.C. designed instruments and experiments, and wrote the manuscript, with H.H. and G.Z.'s assistance. Q.K.X. and Z.C. supervised the project.

## Acknowledgements

This work was supported by the National Key R&D Program of China (No. 2022YFA1403100 and No. 2022YFA1403101), and the Natural Science Foundation of China (Nos. 92265112 and 12374455). Z.C., DL., and J.L. acknowledge the support from Guangdong Provincial Quantum Science Strategic Initiative (No. GDZX2201001). J.L. and Q.Y. acknowledge the support from Guangdong Innovative and Entrepreneurial Research Team Program (Grant No. 2019ZT08C044) and Shenzhen Science and Technology Program (No. 20200925161102001). TEM characterization was performed at the Cryo-EM Center and Pico Center from SUSTech Core Research Facilities that receives support from the Presidential Fund and Development and Reform Commission

of Shenzhen Municipality. D.L. acknowledges the support from Guangdong Basic and Applied Basic Research Grant (No. 2023A1515011352) and Hong Kong Research Grants Council (CityU 21301221, CityU 11309622). Y.S. acknowledges the support from Natural Science Foundation of China (No. 12141402). G.M.Z. acknowledges the support of National Key Research and Development Program of China (Grant No. 2023YFA1406400).

### **Competing interests**

The authors declare no competing interests.

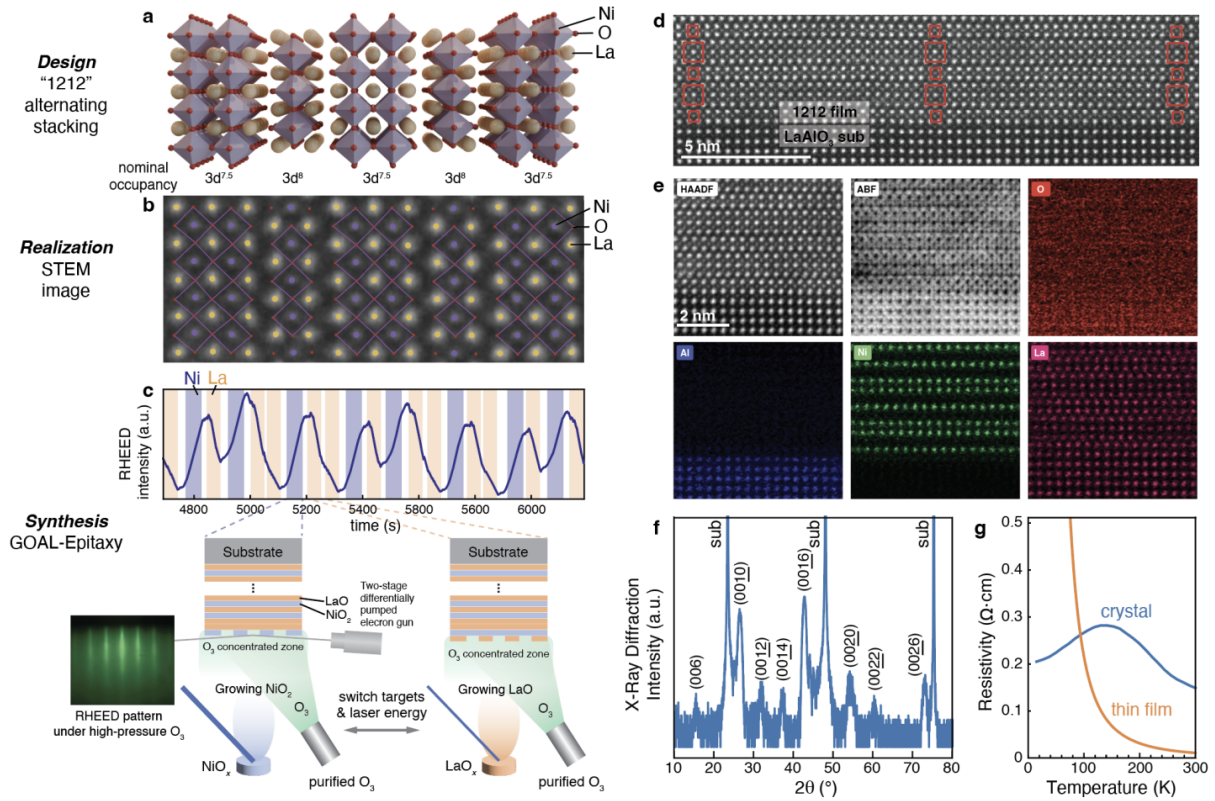


**Fig. 1 | Synthesis of a designed complex structure with gigantic-oxidative atomically layered epitaxy (GOAL-Epitaxy).** **a**, Schematic of a designed complex structure, featuring alternating stacking of single and double layers of  $\text{NiO}_2$  (denoted as “1212”). This structure does not belong to the series of Ruddlesden-Popper phase. **b**, Magnified scanning transmission electron microscopy (STEM) image of the grown film, showing a region of lattice structure that is the same as that depicted in **a**. Atom positions are determined based on both high-angle annular dark field (HAADF) and annular bright field (ABF) images. **c**, Reflective high-energy electron diffraction (RHEED) intensity oscillations as a function of time. Blue and yellow blocks represent durations of  $\text{NiO}_x$  and  $\text{LaO}_x$  targets being ablated, respectively. Lower schematics describe how a complex structure is constructed atomic-layer-by-layer in the GOAL-Epitaxy setup. **d**, Larger-field-of-view HAADF image of the atomically sharp 1212 film and  $\text{LaAlO}_3$  substrate interface. Red squares are guides to the eye for single- $\text{NiO}_2$  structures and double- $\text{NiO}_2$  structures. **e**, HAADF, ABF, and atomically resolved Energy-dispersive X-ray spectroscopy (EDS, for O, Al, Ni, and La, respectively) images of the same region of lattice. Alternating single and double layers of  $\text{NiO}_2$  are exhibited. **f**, X-ray diffraction (XRD) in log scale of a 10-nm 1212 film. **g**, Resistivity as a function of temperature for a 20-nm 1212 film and a crystal.

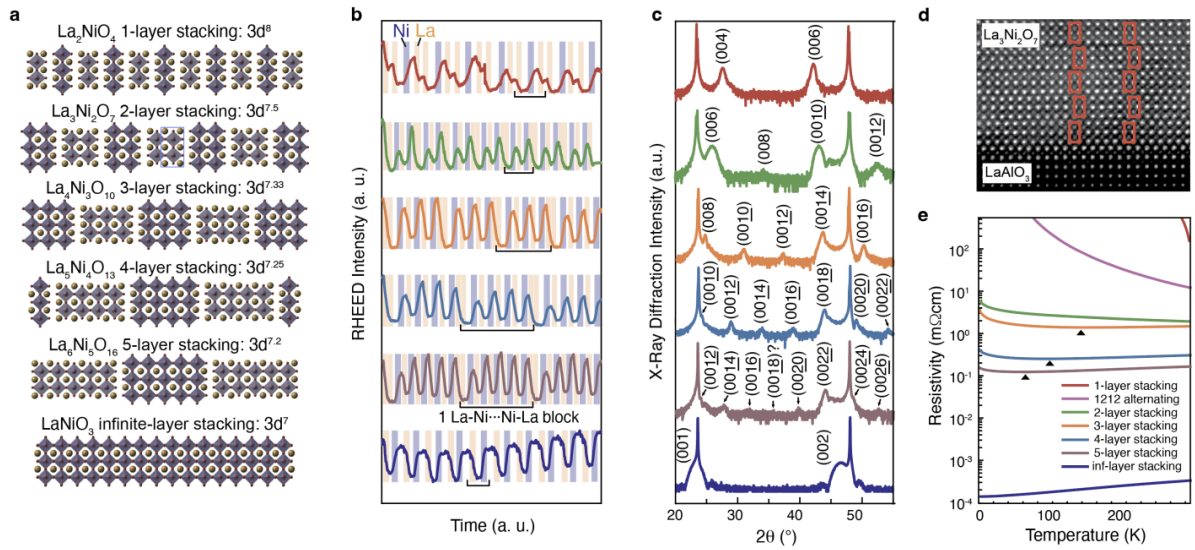


**Fig. 2 | Synthesis of complex nickelate structures with *in situ* reduction.** **a**, Schematic structures of a series of Ruddlesden-Popper phases of nickelates. **b**, RHEED oscillations corresponding to each of the designs in **a**. Blue and yellow blocks represent durations of  $\text{NiO}_x$  and  $\text{LaO}_x$  targets being ablated, respectively. Horizontal time axes are shifted and rescaled for comparisons among different growth. **c**, XRD corresponding to each of the thin film synthesized according to design. Film thickness ranges from 10-20 nm. **d**, STEM HAADF image of a grown double-layer stacking structure,  $\text{La}_3\text{Ni}_2\text{O}_7$ . Red rectangles are guides to the eye highlighting  $\text{LaO-NiO}_2\text{-LaO-NiO}_2\text{-LaO}$  blocks, as a fundamental unit that construct the structure. **e**, Resistivity-versus-temperature curves for varied synthesized films. Black filled triangles indicate where resistivity starts increasing with temperature decrease.



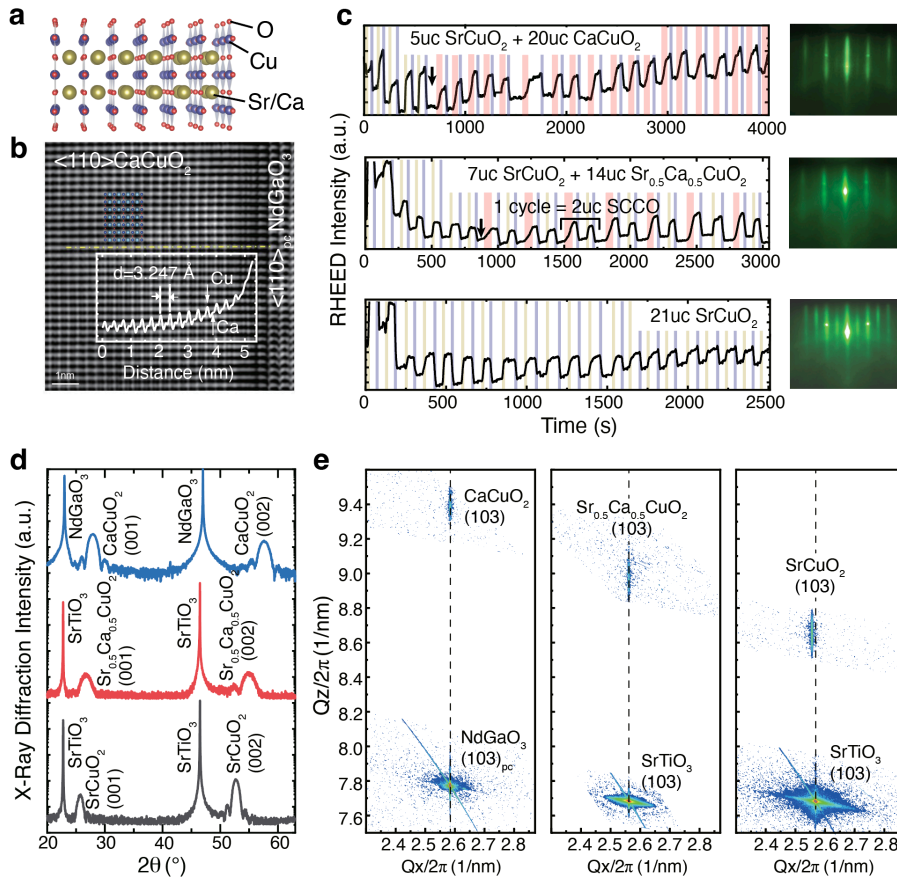


**Fig. 3 | Synthesis of infinite-layer cuprates.** **a**, Schematic lattice structure of infinite-layer cuprates. **b**, STEM image of a  $\text{CaCuO}_2/\text{NdGaO}_3$  sample, with inset showing the image intensity as a function of distance. **c**, Example RHEED oscillations and patterns of  $\text{CaCuO}_2$  growth on  $\text{NdGaO}_3$  substrate with  $\text{SrCuO}_2$  buffer (top),  $\text{Sr}_{0.5}\text{Ca}_{0.5}\text{CuO}_2$  (with  $\text{SrCuO}_2$  buffer, middle) and  $\text{SrCuO}_2$  growth on  $\text{SrTiO}_3$  substrates (bottom). Small arrows indicate the completion of buffer layers. Blue, pink, and yellow blocks represent durations of  $\text{CuO}_x$ ,  $\text{SrO}_x$ , and  $\text{CaO}_x$  targets being ablated, respectively. Note that 1 cycle of sequential depositions of  $\text{CaO}_x$ ,  $\text{CuO}_x$ ,  $\text{SrO}_x$ , and  $\text{CuO}_x$ , corresponding to 2UC  $\text{Sr}_{0.5}\text{Ca}_{0.5}\text{CuO}_2$ . Representative RHEED images shown are taken during growth with Cu termination at thickness of 5 unit-cell (UC)  $\text{SrCuO}_2$  plus 10 UC  $\text{CaCuO}_2$  (top), Sr termination at a thickness of 7 UC  $\text{SrCuO}_2$  plus 4UC  $\text{Sr}_{0.5}\text{Ca}_{0.5}\text{CuO}_2$  (middle), Sr termination at a thickness of 3 UC  $\text{SrCuO}_2$  (bottom). **d** and **e**, XRD spectra along out-of-plane axis and reciprocal space mappings (RSM) of the three samples with growth illustrated in **c**.

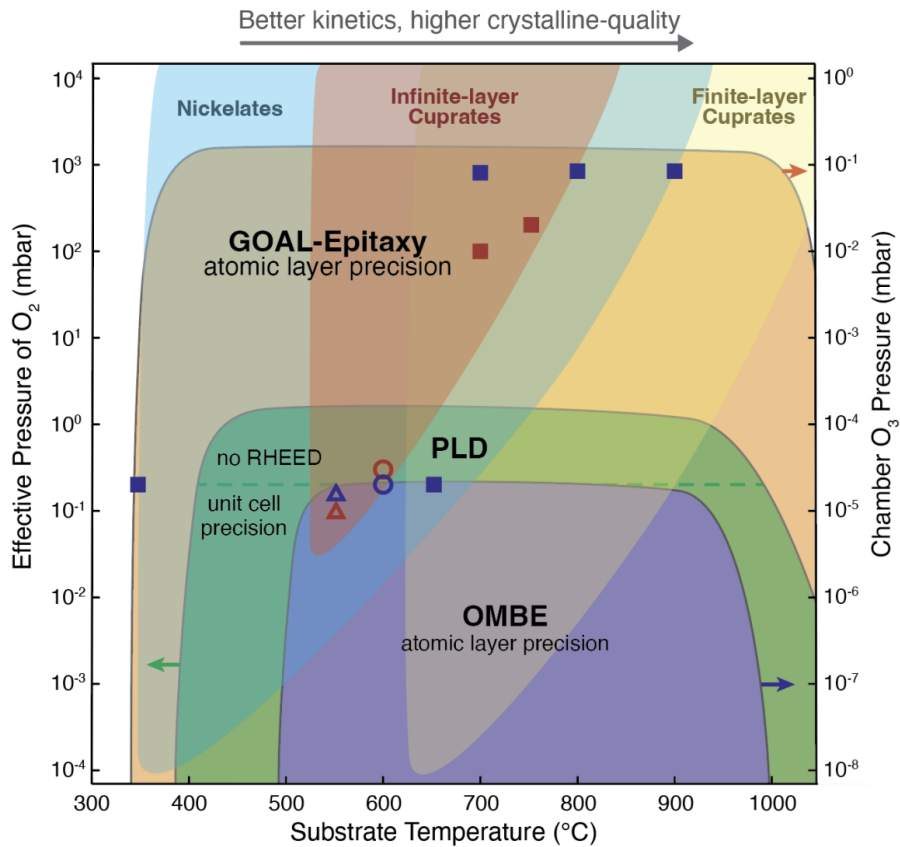


**Fig. 4 | New frontier in synthesis parameter space.** The parameter spaces covered by GOAL-Epitaxy, PLD, and OMBE techniques are represented by orange, green, and blue areas, delineated with solid grey lines, respectively. The parameter spaces where nickelates (here represented by  $\text{ReNiO}_3$ , where  $\text{Re} = \text{rare earth}$ ), infinite-layer cuprates, and finite-layer cuprates (such as  $\text{La}_2\text{CuO}_4$ ,  $\text{YBa}_2\text{Cu}_3\text{O}_{7-\delta}$ , etc.) can be grown are indicated by partially transparent blue, red, and yellow areas without border lines. For the PLD technique, the dashed green line distinguishes the regions where RHEED is applicable or not. Solid squares, empty circles, and empty triangles represent the example growth parameters by GOAL-Epitaxy, PLD<sup>4,34</sup>, and OMBE<sup>30,35,36</sup>, respectively. Blue and red symbols correspond to nickelate and infinite-layer cuprate growth, respectively.